J. Astrophys. Astr. (2023) 44:23
https://doi.org/10.1007/s12036-022-09907-7

STAR FORMATION

Star-forming site RAFGL 5085: Is a perfect candidate of hub-filament system?

L. K. DEWANGAN[1,*], N. K. BHADARI[1,2], A. K. MAITY[1,2], RAKESH PANDEY[1], SAURABH SHARMA[3], T. BAUG[4] and C. ESWARAIAH[5]

[1]Astronomy and Astrophysics Division, Physical Research Laboratory, Navrangpura, Ahmedabad 380009, India.
[2]Indian Institute of Technology Gandhinagar Palaj, Gandhinagar 382355, India.
[3]Aryabhatta Research Institute of Observational Sciences (ARIES), Manora Peak, Nainital 263002, India.
[4]Satyendra Nath Bose National Centre for Basic Sciences, Block-JD, Sector-III, Salt Lake, Kolkata 700106, India.
[5]Indian Institute of Science Education and Research (IISER) Tirupati, Rami Reddy Nagar, Karakambadi Road, Mangalam (P.O.), Tirupati 517507, India.
*Corresponding author. E-mails: loku007@gmail.com; lokeshd@prl.res.in

MS received 15 August 2022; accepted 10 October 2022

Abstract. To investigate the star-formation process, we present a multi-wavelength study of a massive star-forming site RAFGL 5085, which has been associated with the molecular outflow, HII region and near-infrared cluster. The continuum images at 12, 250, 350 and 500 μm show a central region (having $M_{\rm clump} \sim 225\ M_{\odot}$) surrounded by five parsec-scale filaments, revealing a hub-filament system (HFS). In the Herschel column density ($N(H_2)$) map, filaments are identified with higher aspect ratios (length/diameter) and lower $N(H_2)$ values ($\sim$0.1–2.4 $\times$ 10^{21} cm^{-2}), while the central hub is found with a lower aspect ratio and higher $N(H_2)$ values ($\sim$3.5–7.0 $\times$ 10^{21} cm^{-2}). The central hub displays a temperature range of [19, 22.5] K in the Herschel temperature map, and is observed with signatures of star formation (including radio continuum emission). The JCMT ^{13}CO(J = 3–2) line data confirm the presence of HFS and its hub is traced with supersonic and non-thermal motions having higher Mach number and lower thermal to non-thermal pressure ratio. In the ^{13}CO position–velocity diagrams, velocity gradients along the filaments towards the HFS appear to be observed, suggesting the gas flow in the RAFGL 5085 HFS and the applicability of the clump-fed scenario.

Keywords. Dust, extinction—HII regions—ISM: clouds—ISM: individual objects (RAFGL 5085)—stars: formation.

1. Introduction

The role of radiative and mechanical feedback of massive OB stars ($\gtrsim$8 $M_{\odot}$) on the physical environment of their host galaxies has been well known in the literature (e.g., Zinnecker & Yorke 2007; Tan *et al.* 2014; Motte *et al.* 2018). However, despite a great deal of progress in recent years, our understanding on the origin of such massive stars is still incomplete (e.g., Rosen *et al.* 2020). To explain the formation of massive stars, two popular theories, which are the core-fed scenario and the clump-fed scenario, are available in the literature. The core-fed scenario (or monolithic collapse model) supports the existence of massive prestellar cores, where massive stars can form (McKee & Tan 2003). The clump-fed scenario favors the massive stars that are assembled by inflow material from large scales of 1–10 pc clouds outside the cores (Bonnell *et al.* 2001, 2004; Bonnell & Bate 2006; Vázquez-Semadeni *et al.* 2009, 2017, 2019; Padoan *et al.* 2020). To observationally study the formation of massive stars, one needs to explore the embedded morphology and the gas motion around a newly formed massive star that may hold clues to its origin.

This article is part of the Special Issue on "Star formation studies in the context of NIR instruments on 3.6m DOT".

Published online: 28 March 2023

The target site of this paper is a massive star-forming region, RAFGL 5085/IRAS 02461+6147/G136.3833 +02.2666, which is located at a distance of 3.3 kpc (Lumsden *et al.* 2013). RAFGL 5085 has been proposed to host a massive young stellar object (MYSO) with a bolometric luminosity ($L_{\rm bol}$) of 6580 $L_{\odot}$ (Lumsden *et al.* 2013). RAFGL 5085 is associated with very weak centimeter continuum emission (i.e., total flux = 1.7 mJy; Condon *et al.* 1998) and a near-infrared (NIR) cluster (e.g., Carpenter *et al.* 2000; Bica *et al.* 2003). The NIR cluster was identified using the K′ stellar surface density map (see Figure 3 related to IRAS 02461+6147 in Carpenter *et al.* 2000). This cluster was embedded in a molecular ^{12}CO(1–0)/^{13}CO(1–0) condensation/clump (at $V_{\rm lsr} \sim -44$ km s^{-1}; Carpenter *et al.* 2000) traced using the FCRAO outer galaxy ^{12}CO(1–0) survey (Heyer *et al.* 1998). In the direction of the ^{12}CO/^{13}CO clump, dense cores using the C^{18}O(J = 1–0) line data, and compact millimeter continuum sources (MCSs) using the continuum maps at 98 GHz and 110 GHz were reported (Saito *et al.* 2006, 2007). A water maser and the ammonia emission were also detected towards the NIR cluster (Ouyang *et al.* 2019). A bipolar molecular outflow has been investigated towards RAFGL 5085 (e.g., Wu *et al.* 2004; Li *et al.* 2019). Hence, previous observational studies have indicated ongoing star formation activities (including a MYSO) in the target site. However, embedded structure/morphology of the emission at shorter (i.e., NIR and mid-infrared (MIR)) and longer wavelengths (i.e., sub-millimetre (sub-mm)) in RAFGL 5085 is not yet carefully explored. Furthermore, no study is carried out to examine the gas motion towards the previously reported molecular clump hosting RAFGL 5085. This paper focuses in understanding the physical processes underlying star formation in RAFGL 5085 using a multi-wavelength approach, which is yet to be explored. In particular, we have used the Herschel sub-mm images at 250, 350 and 500 μm (e.g., Elia *et al.* 2010; Griffin *et al.* 2010) to produce the dust column-density map and the temperature map in RAFGL 5085, which are not yet studied. This paper also includes the analysis of the ^{12}CO(J = 1–0) and ^{13}CO(J = 3–2) line data.

The paper is organized as follows. Section 2 deals with the observational data sets used in this paper. We present the outcomes extracted from the analysis of multi-wavelength data sets in Section 3. We discuss our findings in Section 4. In Section 5, we present the summary of the work.

2. Data and analysis

Observational data sets at different wavelengths were collected for an area of ∼0.22° × 0.22° (central coordinates: $l = 136.383°$; $b = 2.255°$) around RAFGL 5085 (Table 1). The photometric magnitudes of point-like sources at H and K_s bands were also obtained from the 2MASS point source catalog. Note that the Hi-GAL observations at 70 and 160 μm and Spitzer-GLIMPSE360 map at 3.6 μm do not cover the target site. Hence, these data sets are not available for RAFGL 5085. This work also uses the Gaia early data release 3 (EDR3; Gaia Collaboration *et al.* 2021) based photogeometric distances ('rpgeo') of point-like sources from Bailer-Jones *et al.* (2021).

We also used the bolocam source catalog at 1.1 mm (v2.1; Ginsburg *et al.* 2013) towards RAFGL 5085. From the JCMT Science Archive/Canadian Astronomy Data Centre (CADC), we downloaded the processed JCMT ^{13}CO (3–2) spectral data cube (rest frequency = 330.587960 GHz) and C^{18}O (3–2) line data cube (rest frequency = 329.3305453 GHz) of the

Table 1. List of archival data sets analyzed in this paper.

Survey/data source	Wavelength/ Frequency/line (s)	Resolution (″)	Reference
NRAO VLA Sky Survey (NVSS)	1.4 GHz	∼45	Condon *et al.* (1998)
Milky Way Imaging Scroll Painting (MWISP)	^{12}CO(J = 1–0)	∼50	Su *et al.* (2019)
James Clerk Maxwell Telescope (JCMT)	^{13}CO(J = 3–2), C^{18}O (3–2)	∼14	Buckle *et al.* (2009)
Bolocam Galactic Plane Survey (BGPS)	1.1 mm	∼33	Aguirre *et al.* (2011)
Herschel Infrared Galactic Plane Survey (Hi-GAL)	250, 350, 500 μm	∼18, 25, 37	Molinari *et al.* (2010)
Wide-Field Infrared Survey Explorer (WISE)	12, 22 μm	∼6.5, ∼12	Wright *et al.* (2010)
Spitzer Galactic Legacy Infrared Mid-Plane Survey Extraordinaire 360 (GLIMPSE 360)	4.5 μm	∼2	Whitney *et al.* (2011)
Two Micron All Sky Survey (2MASS)	1.65, 2.2 μm	∼2.5	Skrutskie *et al.* (2006)

object 'G136.3833+02.2666/RAFGL5085' (proposal id: M08BU18), which are calibrated in antenna temperature. The observations (integration time = 59.358 s (for ^{13}CO) and 59.290 s (for C^{18}O)) were taken using the Heterodyne Array Receiver Program/Auto-Correlation Spectral Imaging System (HARP/ACSIS; Buckle *et al.* 2009) spectral imaging system. The pixel scale and resolution of the JCMT line cube are ∼7.″3 and ∼14″, respectively.

3. Results

3.1 *Physical environments around RAFGL 5085*

In the direction of the selected area, the Spitzer 4.5 μm image displays the bright extended emission or diffuse nebulosity (Figure 1a). At least three point-like sources and an elongated feature are found toward the central region of the bright diffuse nebulosity, which hosts the location of RAFGL 5085 (see the inset in Figure 1a). In general, star formation activities can be inferred from the presence of infrared-excess sources and outflow activities. Such infrared-excess sources are generally identified by their varying emission at different infrared bands. Due to the absence of the Spitzer 3.6 μm image, the color conditions based on 3.6 and 4.5 μm bands cannot be used in RAFGL 5085 (e.g., Gutermuth *et al.* 2009). Hence, we have used the 2MASS NIR data to infer the infrared-excess source candidates in our selected target area. In Figure 1(a), we have overlaid the positions of the 2MASS point-like sources having H−K$_s$ > 0.65 (see open circles) on the Spitzer 4.5 μm image. This color condition is chosen based on the analysis of sources associated with a nearby control field. Hence, the 2MASS sources with H–K$_s$ > 0.65 may be considered as infrared-excess source candidates.

Figure 1(b) displays the WISE 12 μm image, revealing at least five filamentary features (length >1 pc) directed toward the central region hosting the location of RAFGL 5085. In the WISE image, a bright source is also seen towards the central region, which does not appear as a point-like source. The dust continuum emission at 1.1 mm is distributed towards the WISE bright source (Figure 1b). We have also examined the distance distribution of Gaia point-like sources in the direction of our selected target area. We found a peak of distance distribution around 3.5 ± 0.36 kpc (see the inset in Figure 1b), which is in agreement with our adopted distance to the target source.

We found a clump in the bolocam 1.1 mm map (Figure 1b) and its total flux at 1.1 mm has been reported to be 1.824 Jy (Ginsburg *et al.* 2013). We have also computed the total mass of the clump using the following formula (Hildebrand 1983; Dewangan *et al.* 2016):

$$M_c = \frac{D^2 S_\nu R_t}{B_\nu(T_d)\kappa_\nu}, \quad (1)$$

where S_ν is the total flux at 1.1 mm (Jy), D is the distance (kpc), R_t is the gas-to-dust mass ratio (assumed to be 100), B_ν is the Planck's function for a dust temperature T_d and κ_ν is the dust absorption coefficient. The analysis uses S_ν = 1.824 Jy (Ginsburg *et al.* 2013), κ_ν = 1.14 cm^2 g^{-1} (Enoch *et al.* 2008; Bally *et al.* 2010), D = 3.3 kpc and T_d = 22 K (Figure 4b). Using these values, we have computed the mass of the bolocam clump to be ∼225 $M_\odot$. This M_c value is estimated to be ∼255 $M_\odot$ at D = 3.5 kpc. We assume an uncertainty on the estimate of the clump mass to be typically ∼20% and at most ∼50%, which could be contributed from the error on the adopted dust temperature, opacity, measured flux and distance of the source.

In Figure 1(c), using the MWISP ^{12}CO(J = 1–0) line data, a molecular condensation is traced towards the bolocam clump, and is depicted in a velocity range of [−46.5, −38.1] km s^{-1}. The NVSS 1.4 GHz continuum emission is also observed towards the WISE bright source (Figure 1d). The filamentary features become more prominent in the Herschel images at 250 and 350 μm (Figure 1e and f). Overall, multi-wavelength images suggest the existence of a hub-filament system (HFS; i.e., a convergence of filaments towards the compact and dense hub). Interestingly, the ionized emission and infrared-excess source candidates are evident towards the central hub of the HFS (or RAFGL 5085 HFS).

Note that the MWISP ^{12}CO(J = 1–0) line data do not resolve the HFS as seen in the WISE and Herschel images due to a coarse beam size. Hence, we examined the high resolution JCMT ^{13}CO(J = 3–2) and C^{18}O(J = 3–2) line data (resolution ∼14″). However, the JCMT line observations do not cover the entire area as presented in Figure 1(a) and are available for a region highlighted by a solid box in Figure 1(f). In Figure 2(a), we display the JCMT ^{13}CO(J = 3–2) integrated intensity (moment-0) map (at [−45.35, −39.48] km s^{-1}), which reveals a central molecular condensation surrounded by parsec-scale molecular filaments. Figure 2(b) shows the Spitzer 4.5 μm image overlaid with the JCMT ^{13}CO emission contours. The bright diffuse nebulosity traced in the Spitzer 4.5 μm image is seen towards the central molecular condensation, which is surrounded by molecular filaments. Five arrows 't1–t5'

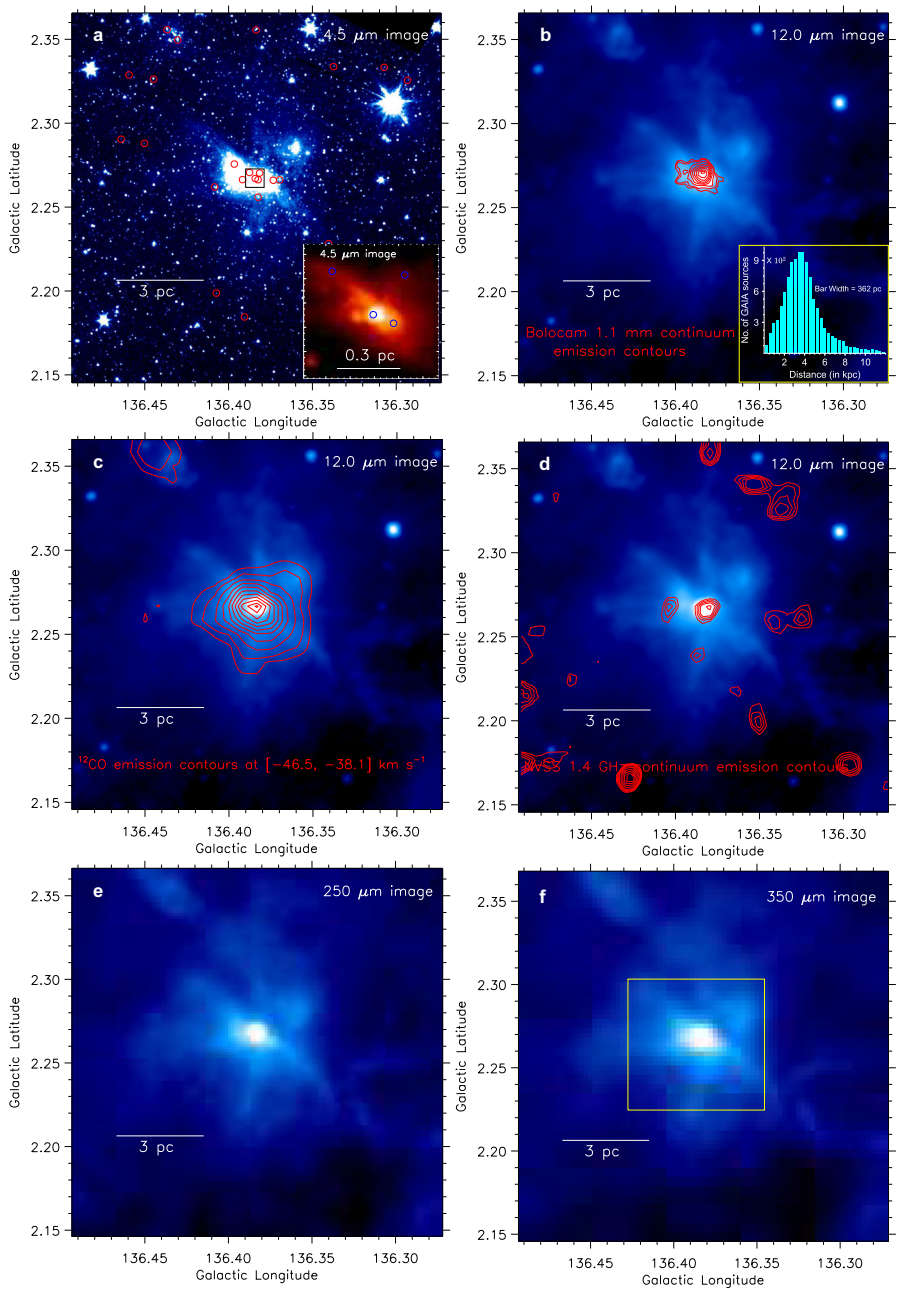

Figure 1. Multi-wavelength view of RAFGL 5085. The images are shown at different wavelengths, which are highlighted in the panels. (a) Overlay of infrared-excess source candidates with H–K_s > 0.65 (see red circles) on the Spitzer 4.5 μm image. Using the Spitzer 4.5 μm image, a zoomed-in view of the central region is shown using the inset on the bottom right (see a solid box in Figure 1a). Infrared-excess source candidates are also indicated by circles. (b) Overlay of the bolocam 1.1 mm continuum emission contours on the WISE 12 μm image, and the levels of the contours are 0.697 Jy per beam× (0.25, 0.3, 0.4, 0.5, 0.6, 0.7, 0.8, 0.9, 0.98). The inset on the bottom right shows the distance distribution of Gaia point-like sources towards our selected target area. (c) Overlay of the MWISP ^{12}CO (1–0) emission contours at [−46.5, −38.1] km s^{-1} on the WISE 12 μm image, and the levels of the contours are 63.1 K km s^{-1}× (0.07, 0.12, 0.2, 0.3, 0.4, 0.5, 0.6, 0.7, 0.8, 0.9, 0.98). (d) Overlay of the NVSS 1.4 GHz radio continuum emission contours on the WISE 12 μm image, and the levels of the contours are 2.467 mJy per beam× (0.35, 0.4, 0.45, 0.5, 0.6, 0.7, 0.8, 0.9, 0.98). (e) The panel shows the Herschel 250 μm image. (f) The panel displays the Herschel 350 μm image. A solid box highlights the area shown in Figure 2(a and b). In all panels, a scale bar (at a distance of 3.3 kpc) is presented.

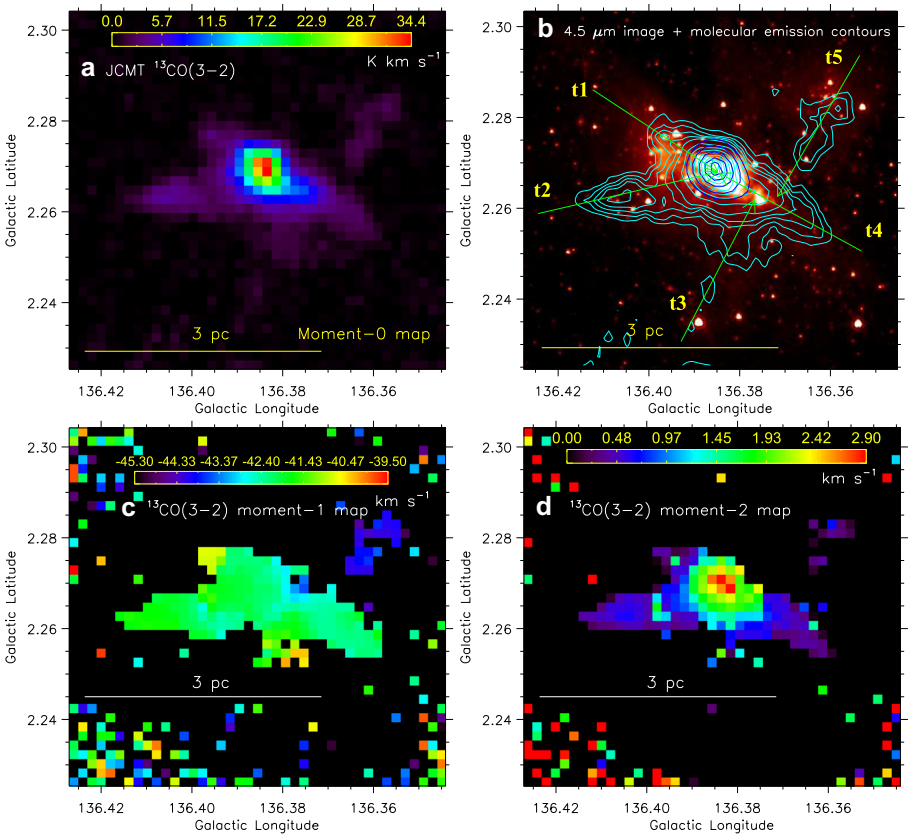

Figure 2. (a) The panel shows JCMT ^{13}CO(J = 3–2) integrated intensity (moment-0) map (at [−45.35, −39.48] km s^{-1}) of an area hosting the target site (see a box in Figure 1f). (b) Overlay of the ^{13}CO(J = 3–2) emission contours on the Spitzer 4.5 μm image. The ^{13}CO(J = 3–2) contours (in cyan) are 34.13 K km s^{-1} × (0.03, 0.05, 0.07, 0.09, 0.12, 0.2, 0.3, 0.4, 0.5, 0.6, 0.7, 0.8, 0.9, 0.98). Solid blue contours of the JCMT C^{18}O(J = 3–2) integrated intensity map (at [−45.35, −39.48] km s^{-1}) are also presented with the levels of 1, 1.5, 2.1, 2.6 and 2.9 K km s^{-1}. Five arrows 't1–t5' are marked in the panel, where the position–velocity diagrams are generated (Figure 5a–e). (c) The panel shows the line-of-sight velocity map (moment-1 map) of the JCMT ^{13}CO(J = 3–2) emission. (d) JCMT ^{13}CO(J = 3–2) intensity-weighed FWHM line width map (moment-2 map). A scale bar corresponding to 3 pc (at a distance of 3.3 kpc) is shown in each panel.

highlight the molecular filaments. The JCMT C^{18}O(J = 3–2) emission contours are also overlaid on the Spitzer 4.5 μm image, and are mainly distributed towards the central hub of the HFS. We do not detect any C^{18}O emission towards the molecular filaments as seen in the ^{13}CO map. Collectively, the JCMT ^{13}CO(J = 3–2) moment-0 map also supports the existence of HFS.

Apart from the integrated intensity map/moment-0 map, we have also examined the intensity-weighed mean velocity/moment-1 map and the intensity-weighed velocity dispersion/intensity-weighed line width/moment-2 map of ^{13}CO(J = 3–2). Concerning these moment maps, one needs to collapse the data cube along the spectral axis by taking a moment of the data. The complete mathematical expressions of these moments are given in Teague (2019). In Figure 2(c and d), the line-of-sight velocity map (moment-1 map) of ^{13}CO(J = 3–2) and the intensity-weighed Full Width Half Maximum (FWHM) line width map (moment-2) of ^{13}CO(J = 3–2) are presented. Some velocity variations may be inferred towards the HFS. Higher line widths are evident towards the central hub compared to the filaments (see Section 3.4). All these moment maps are produced along the spectral axis from the Python package SpectralCube.[1]

3.2 *Identification of filament skeletons and their configuration*

To reveal the structures of filaments or filamentary skeletons, we employed the 'getsf' (Men'shchikov 2021) algorithm on the Herschel 250 μm image. This particular image has better spatial resolution compared to other Herschel images at 350 and 500 μm. The algorithm distinguishes the structural components from their backgrounds in a given astronomical image.

[1] https://spectral-cube.readthedocs.io/en/latest/moments.html.

It requires the input of maximum width of filament (i.e., FWHM in arcsec), which the user wants to extract (see Bhadari *et al.* 2022, for the detailed steps). However, the output files include the scale dependent (i.e., from the image resolution scale to the maximum width of filaments) skeletons within the range of the user's scale of interest. The filament skeletons identified on the scale of 51″ are presented in Figure 3(a). To run the 'getsf', we set the maximum filament width size of 60″. Figure 3(b) is the same as Figure 3(a), but it also shows the ^{13}CO(J = 3–2) emission contours (Figure 2b). In Figure 3(a and b), the HFS and its association with molecular gas are evident.

3.3 *Herschel column density and temperature maps*

Figure 4(a and b) show the Herschel column density and temperature maps (resolution ∼37″), respectively. Following the methods described in Mallick *et al.* (2015), these Herschel maps are produced using the Hi-GAL continuum images at 250, 350 and 500 μm. Note that the Herschel 160 μm image is not used in the analysis due to its unavailability. The Herschel column density and temperature maps are generated from a pixel-by-pixel spectral energy distribution (SED) fit with a modified blackbody to the sub-mm emission at 250–500 μm. A background flux level was estimated for each sub-mm wavelength, and is determined to be 0.18, 0.13 and 0.06 Jy per pixel for the 250, 350 and 500 μm images (size of the selected featureless dark region ∼9′ × 9′; centered at: l = 135.412°; b = 2.092°), respectively. In this analysis, we considered a mean molecular weight per hydrogen molecule (μ_{H2}) of 2.8 (Kauffmann *et al.* 2008), an absorption coefficient (κ_ν) of 0.1 $(\nu/1000\ \mathrm{GHz})^\beta$ cm^2 g^{-1} with a dust spectral index (β) of 2 (see Hildebrand 1983), and a gas-to-dust ratio of 100. The HFS is not very prominent in the Herschel column density map, but the central hub is associated with warm dust emission (T_d ∼ 19–22.5 K). Uncertainties on the estimate of the column densities and the dust temperatures could be ∼10–20% (e.g., Launhardt *et al.* 2013).

Figure 4(c) presents filaments identified by 'getsf' on the Herschel 250 μm image (Figure 3a), which are utilized to mask the column density map as shown in Figure 4(a). Figure 4(c) exhibits filaments with high aspect ratios (length/diameter) and lower column densities (∼0.1–2.4 × 10^{21} cm^{-2}), while the central hub is found with a low aspect ratio and high column density (∼3.5–7.0 × 10^{21} cm^{-2}). Figure 4(d) is same as Figure 4(c), but it also displays the ^{13}CO(J = 3–2) emission contours (Figure 2b). We found the spatial connection of molecular gas with the structures seen in the column density map (Figure 4d).

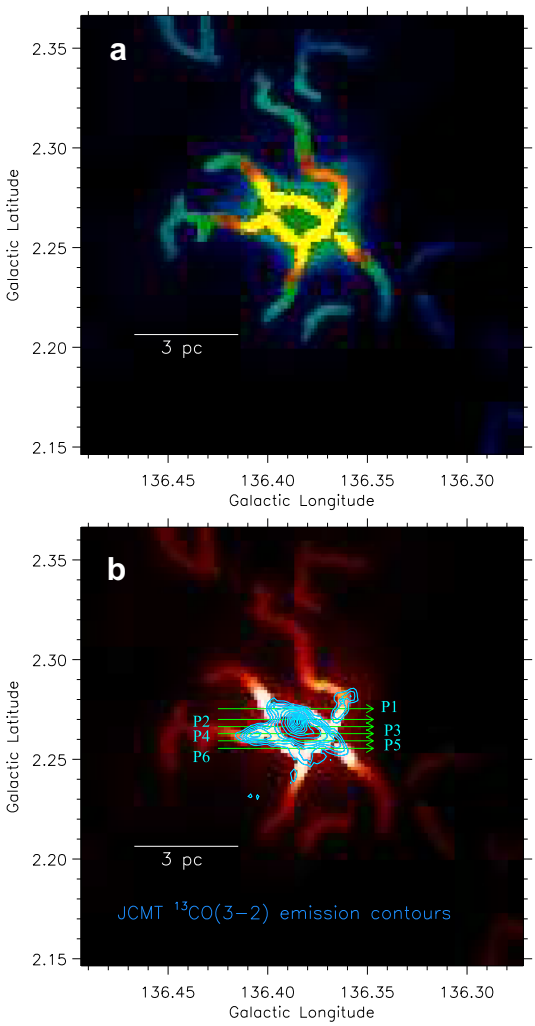

Figure 3. (a) The panel shows the emission skeletons (on the scale of 51″) identified from the Herschel 250 μm image (resolution ∼18″) using the algorithm 'getsf'. (b) Same as Figure 3(a), but it is overlaid with the ^{13}CO(J = 3–2) contours (Figure 2b). Six arrows 'p1–p6' are indicated in the panel, where the position–velocity diagrams are generated (Figure 6a–f). A scale bar corresponding to 3 pc (at a distance of 3.3 kpc) is shown in each panel.

3.4 *JCMT position–velocity diagrams and non-thermal velocity dispersion map*

As mentioned earlier, the JCMT molecular line data do not cover the entire HFS as traced in the Herschel

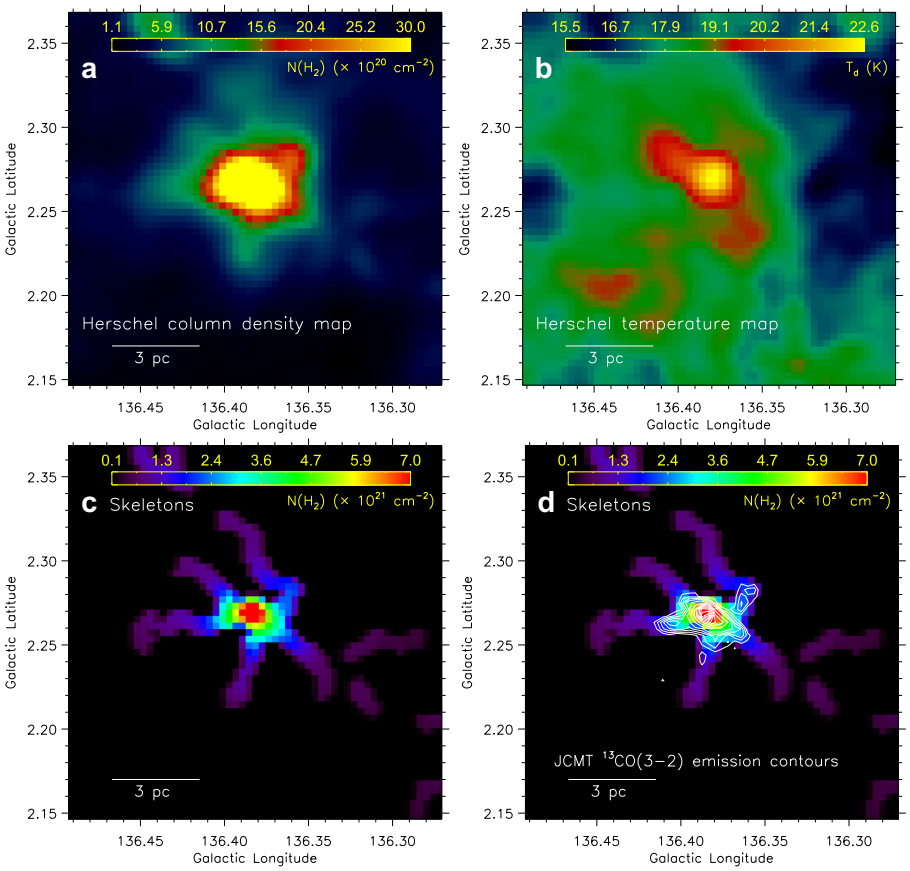

Figure 4. (a) The panel displays the Herschel column density map (resolution ∼37″) of an area presented in Figure 1(a). (b) The panel shows the Herschel temperature map (resolution ∼37″). (c) The panel displays filaments identified on the Herschel 250 μm by the algorithm 'getsf' (Men'shchikov 2021), which are utilized to mask the column density map as shown in Figure 4(a). (d) Same as Figure 4(c), but it is overlaid with the ^{13}CO(J = 3–2) contours (Figure 2b). A scale bar corresponding to 3 pc (at a distance of 3.3 kpc) is shown in each panel.

maps, and are available for the central area of the HFS (Figure 3b). Hence, to examine the gas motion towards the HFS, we have produced position–velocity diagrams along several paths passing through the molecular filaments and the central hub (see five arrows t1–t5 in Figure 2b and six horizontal arrows p1–p6 in Figure 3b). The arrows t1–t5 are selected towards the molecular filaments, and in such paths, we take the outermost edge of each filament as the reference point and go towards the central hub. On the other hand, the horizontal arrows p1–p6 pass through the central hub and some molecular filaments. Hence, the paths t1–t5 and the paths p1–p6 may pass through the common areas of the HFS.

Position–velocity diagrams along arrows t1–t5 are presented in Figure 5(a–e). These diagrams hint at the presence of a noticeable velocity gradient along the molecular filaments (Figure 5b, d and e). In the direction of the filament 't2', a velocity gradient is determined to be about 1.6 km s^{-1} pc^{-1}. In Figure 6(a–f), we also display the position–velocity diagrams along arrows p1–p6. The arrows p2–p4 seem to pass through the central hub of HFS (see also the arrow 't2' in Figure 2b), and the position–velocity maps along these paths suggest the outflow activity associated with the central hub (Figure 6b–d), where infrared-excess source candidates are observed. Two arrows p4 and p5 appear to pass through the molecular filaments of the HFS, and one can see a noticeable velocity gradient along the molecular filaments toward the HFS in the position–velocity maps (Figure 6d, e and Figure 5b). Considering all these maps, there is a hint of the presence of velocity gradient toward the HFS. To further carry out such a study, high resolution molecular line observations for a wide area around RAFGL 5085 will be required.

We have also utilized the JCMT ^{13}CO(J = 3–2) line data to infer the non-thermal velocity dispersion, sound speed, Mach number, ratio of thermal to non-thermal pressure towards the molecular features traced in the JCMT moment-0 map. An expression of the

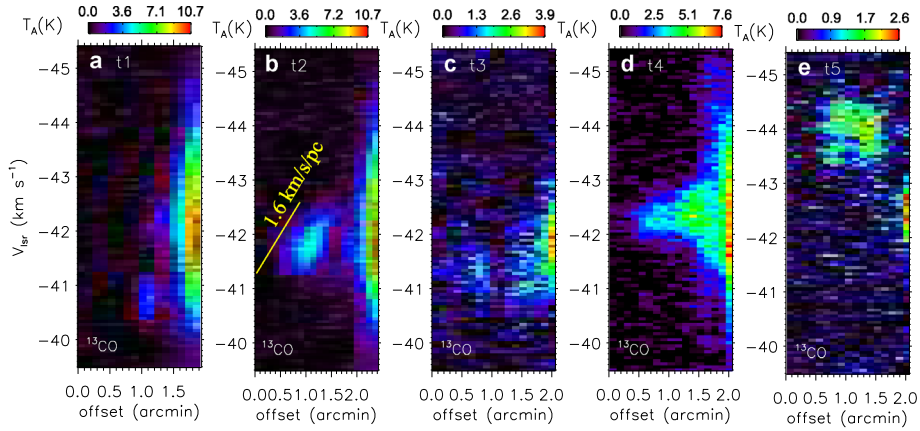

Figure 5. Position–velocity diagrams of the ^{13}CO(J = 3–2) emission along arrows (a) 't1'; (b) 't2'; (c) 't3'; (d) 't4'; (e) 't5' (see arrows in Figure 2b). In panel 'b', a reference bar at 1.6 km s^{-1} pc^{-1} is marked to show a velocity gradient.

non-thermal velocity dispersion is defined below:

$$\sigma_{\rm NT} = \sqrt{\frac{\Delta V^2}{8\ln 2} - \frac{kT_{\rm kin}}{29m_{\rm H}}} = \sqrt{\frac{\Delta V^2}{8\ln 2} - \sigma_T^2}, \qquad (2)$$

where ΔV is the measured FWHM line width, $\sigma_T (= (kT_{\rm kin}/29m_{\rm H})^{1/2})$ is the thermal broadening for ^{13}CO at gas kinetic temperature ($T_{\rm kin}$) and $m_{\rm H}$ is the mass of hydrogen atom. Mach number can also be determined by taking the ratio of non-thermal velocity dispersion ($\sigma_{\rm NT}$) to sound speed (a_s). An expression of the sound speed is $a_s = (kT_{\rm kin}/\mu m_H)^{1/2}$, where μ is the mean molecular weight ($\mu = 2.37$; ~70% H and 28% He by mass). Such estimates also allow us to compute the ratio of thermal to non-thermal (or turbulent) pressure (Lada *et al.* 2003), and its expression is $R_p = a_s^2/\sigma_{\rm NT}^2$. Note that we do not have the knowledge of $T_{\rm kin}$. Hence, dust temperature is used in the calculation, and is taken from the Herschel temperature map (Figure 4b).

In Figure 7(a), we displayed the moment-2 map of ^{13}CO(J = 3–2) overlaid with the contours of dust temperature at [18.5, 19.0, 19.5, 20.0, 20.5, 21.0, 21.5, 22.0, 22.5] K. Figure 7(b, c and d) show the JCMT ^{13}CO(J = 3–2) $\sigma_{\rm NT}$ map, Mach number map and R_p map, respectively. In the direction of the central hub, the values of ΔV, $\sigma_{\rm NT}$ and Mach number are larger than other molecular features. Furthermore, a smaller value of R_p (<1) is found towards the central hub, suggesting that the non-thermal pressure is higher than the thermal pressure in the hub.

4. Discussion

To examine a wider scale environment of our selected target area containing the site RAFGL 5085, we present a color–composite map (250 μm (in red), 22 μm (in green) and 12 μm (in blue) images), which is also overlaid with the NVSS 1.4 radio-continuum emission. The HII regions associated with the sites S192 and S196 are seen, and their physical separations from our target site RAFGL 5085 are also indicated in Figure 8. The extended MIR emission is traced towards the sites S192 and S196, while the compact MIR emission is found towards RAFGL 5085. From Figure 8, we notice that RAFGL 5085 appears to be located between the two evolved HII regions S192 and S196.

Previously, the NIR cluster—associated with the outflow signature, massive star formation and water maser—has been reported towards the molecular and dust clump hosting the location of RAFGL 5085 (Carpenter *et al.* 2000; Wu *et al.* 2004; Saito *et al.* 2006, 2007; Lumsden *et al.* 2013; Li *et al.* 2019; Ouyang *et al.* 2019), where dense molecular cores have been identified (e.g., Saito *et al.* 2006). Due to the detection of weak radio continuum emission (i.e., total flux = 1.7 mJy; Condon *et al.* 1998), we do not favor the presence of any evolved HII region in RAFGL 5085. Hence, the site RAFGL 5085 seems to be associated with an early stage of massive star formation (see also Lumsden *et al.* 2013). In this paper, using the Herschel sub-mm images and the WISE image at 12 μm, our findings reveal a new picture in RAFGL 5085, which is the existence of a HFS. In this connection, the algorithm 'getsf' identified at least five filaments (having $N(H_2) \sim 0.1$–2.4×10^{21} cm^{-2}), which appear to direct to the central hub (having $N(H_2) \sim 3.5$–7.0×10^{21} cm^{-2}). This finding is also supported by the JCMT ^{13}CO(J = 3–2) line data. All the signatures of star formation (including radio-continuum emission) are found towards the central hub of the HFS (see Section 3.1), where higher values of

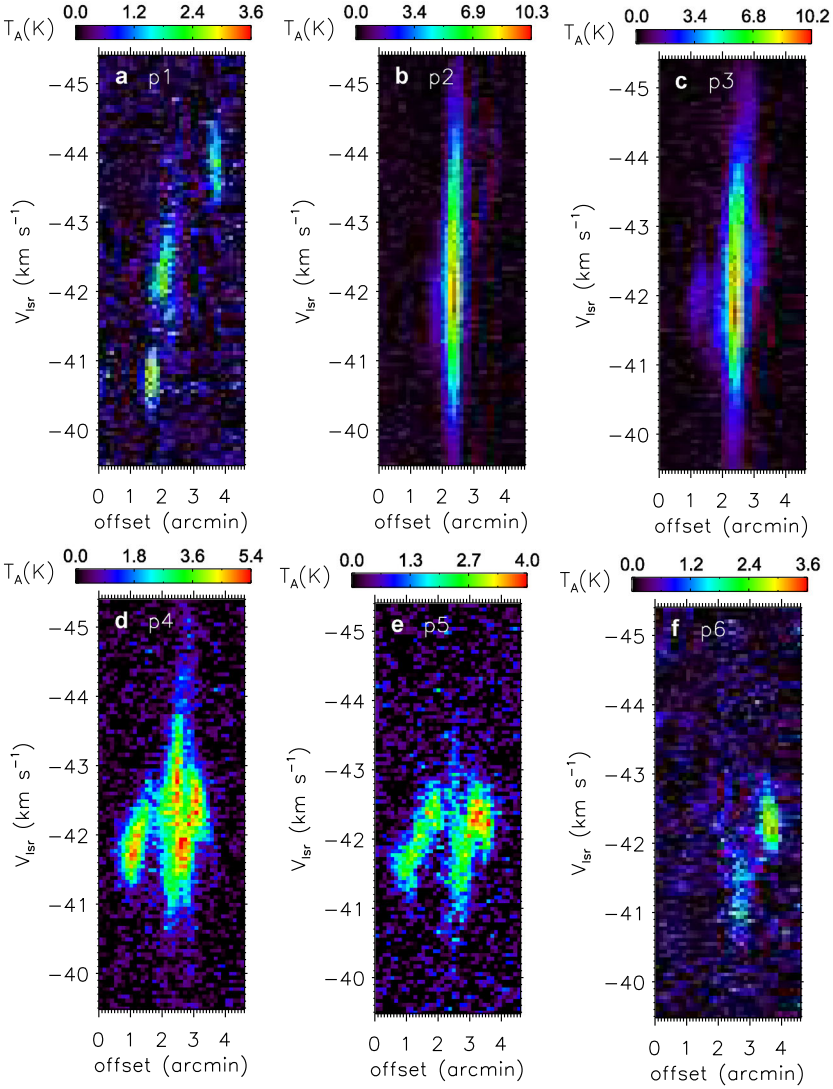

Figure 6. Position–velocity diagrams of the ^{13}CO(J = 3–2) emission along arrows (a) 'p1'; (b) 'p2'; (c) 'p3'; (d) 'p4'; (e) 'p5'; (f) 'p6' (see arrows in Figure 3b).

Mach number and non-thermal pressure are depicted (see Section 3.4).

Prior to the Herschel era, HFSs hosting protoclusters were studied by Myers (2009). After the availability of the Herschel sub-mm maps, to understand the process of mass accumulation in MSF, the study of HFS and its implication has received considerable attention (e.g., Motte *et al.* 2018). In hub-filament configurations, it is thought that filaments are instrumental in channeling interstellar gas and dust to the central hub, where massive stars are assembled by the inflow material (André *et al.* 2010; Schneider *et al.* 2012; Motte *et al.* 2018; Treviño-Morales *et al.* 2019; Rosen *et al.* 2020). In this context, velocity gradients (e.g., 0.5–2.5 km s^{-1} pc^{-1}) along with molecular filaments have been observed in HFSs, and are suggested as a signature of gas accretion along the filaments (Kirk *et al.* 2013; Nakamura *et al.* 2014; Olmi *et al.* 2016; Hacar *et al.* 2017; Baug *et al.* 2018; Treviño-Morales *et al.* 2019; Chen *et al.* 2020; Dewangan *et al.* 2020). Such material/gas flow is thought to feed star-forming cores and proto-clusters in the hub (e.g., Treviño-Morales *et al.* 2019). The earlier reported velocity gradients in the filaments were determined to be higher than the sound speed of ∼0.2 km s^{-1} at $T = 10$ K, indicating a flow of turbulent gas (e.g., Baug *et al.* 2018). The presence of a velocity gradient towards the HFS is found (Figures 5 and 6), hinting gas flow along filaments to the central hub. However, we do not have enough molecular line data for the entire HFS to further probe the velocity gradients (e.g., Hacar & Tafalla 2011; Hacar *et al.* 2013). Hence, this demands new high-resolution and high-sensitivity molecular line data for a wide area around the RAFGL 5085 HFS to further confirm our proposed argument. The detection of

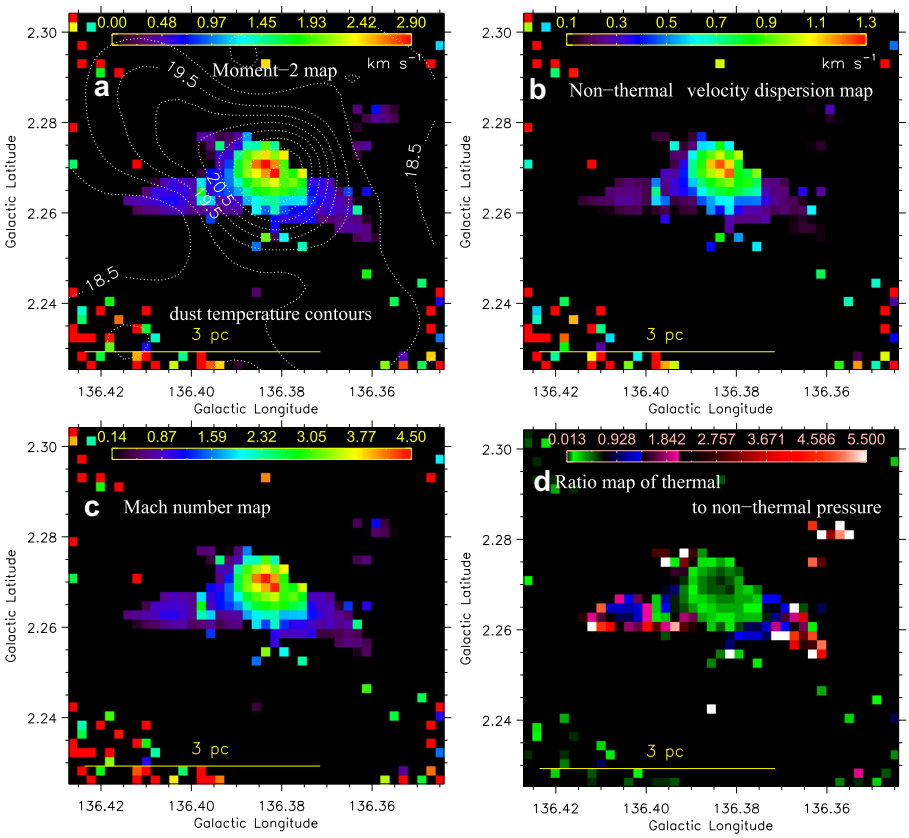

Figure 7. (a) JCMT ^{13}CO(J = 3–2) moment-2 map (see also Figure 2d). The contours of dust temperature at [18.5, 19.0, 19.5, 20.0, 20.5, 21.0, 21.5, 22.0, 22.5] K are also overlaid on the moment-2 map (see also Figure 4b). (b) JCMT ^{13}CO(J = 3–2) non-thermal velocity dispersion map. (c) JCMT ^{13}CO(J = 3–2) Mach number map. (d) JCMT ^{13}CO(J = 3–2) ratio map of thermal to non-thermal (or turbulent) pressure.

a hub-filament configuration supports the applicability of the clump-fed scenario as discussed in the 'Introduction' section. In the clump-fed scenario, inflow material from very large scales of 1–10 pc is thought to be responsible for the birth of massive stars. Such inflow material can be gravity-driven or are produced due to supersonic turbulence (e.g., Motte *et al.* 2018; Padoan *et al.* 2020; Liu *et al.* 2022). With the available data sets mentioned in Table 1, the detailed study of this proposed aspect is outside the scope of this paper.

Based on gravity-driven inflow, an evolutionary scheme has been proposed to explain the birth of massive stars (Tigé *et al.* 2017; Motte *et al.* 2018). This scheme does not favor the existence of high-mass prestellar cores. Rather, low-mass prestellar cores are suggested to develop first (within $\sim 10^4$ years) in the starless phase of massive dense cores/clumps (MDCs, in a 0.1 pc scale). The protostellar phase of MDCs begins when the low-mass protostellar core forms. The local ($\sim$0.02 pc) collapse of these cores is accompanied by the global ($\sim$0.1–1 pc) collapse of MDCs and hub region. In this way, the low-mass protostellar core gains mass

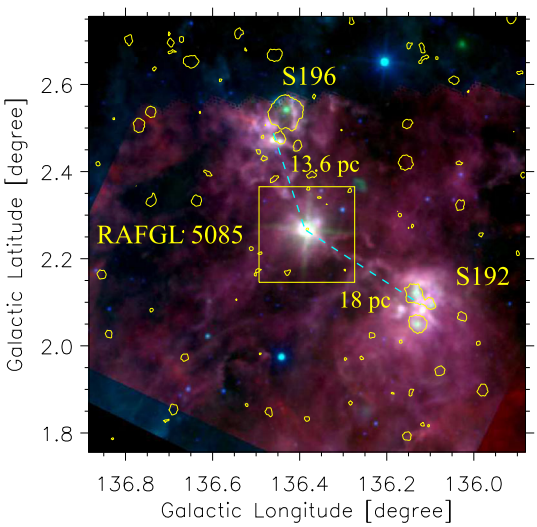

Figure 8. Large-scale view of an area containing the site RAFGL 5085. The panel displays a 3-color composite map made using the Herschel 250 μm (in red), WISE 22 μm (in green) and WISE 12 μm (in blue) images. The NVSS 1.4 GHz radio-continuum emission contour at 1.35 mJy per beam is also overlaid on the color composite map. The target area of this paper is indicated by a dotted–dashed box.

from these gravity-driven inflows and becomes a high-mass protostar ($\sim 3 \times 10^4$ yrs). In the later stage, the scheme favors the development of HII regions around massive protostars with masses $>8\ M_\odot$. The HII region forms when the strong UV field from a massive protostar ionizes the protostellar envelope. Simultaneously, the main accretion phase also terminates. According to this scheme, one may expect simultaneous growth of stars, cores and ridges from the mass of their parental cloud.

The HFSs are very common structures in the massive star-forming sites, but a perfect hub-filament configuration is not often seen in most cases. This is because of the stellar feedback from HII regions (or proto clusters) which gradually destroys the HFS as the proto cluster evolves (see Baug *et al.* 2015, 2018; Dewangan *et al.* 2017, 2020, 2022; Treviño-Morales *et al.* 2019; Dewangan 2021, 2022). It seems that the observed RAFGL 5085 HFS is not yet influenced by UV radiation from the HII region. Hence, our target source RAFGL 5085 appears to be one of the perfect HFS candidates, where the young sources (including massive protostar) are found to be formed in the hub region.

5. Conclusion and summary

In this paper, using a multi-wavelength approach, the physical environment of a massive star-forming site RAFGL 5085 has been studied. Our visual inspection of the continuum images at 12, 250, 350 and 500 μm has revealed a hub-filament configuration, which consists of a central region ($M_{\rm clump} \sim 225\ M_\odot$) surrounded by at least five parsec-scale filaments. We also applied the getsf tool in the Herschel sub-mm images to extract filaments, and their observed configuration supports the presence of the HFS in the site RAFGL 5085. In the Herschel column-density map, filaments are identified with higher aspect ratios (length/diameter) and lower $N(H_2)$ values ($\sim$0.1–2.4 $\times\ 10^{21}$ cm^{-2}), while the central hub is found with a lower aspect ratio and higher $N(H_2)$ values ($\sim$3.5–7.0 $\times\ 10^{21}$ cm^{-2}). The central hub of the RAFGL 5085 HFS is associated with warmer dust emission (i.e., $T_{\rm d} \sim [19, 22.5]$ K). Signposts of star formation (including radio-continuum emission) are concentrated towards the central hub. Our analysis of the JCMT ^{13}CO(J = 3–2) line data also confirms the presence of the HFS in RAFGL 5085. One can note that the JCMT molecular line data are not available for the entire HFS as found in the Herschel maps, and cover mainly the central area of the HFS. The central hub is traced with supersonic and non-thermal motions having higher Mach number and lower thermal to non-thermal pressure ratio. In the ^{13}CO(J = 3–2) position–velocity diagrams, velocity gradients along the filaments towards the HFS seem to be present, suggesting the gas flow in the RAFGL 5085 HFS and the applicability of the clump-fed scenario. We also suggest that the site RAFGL 5085 hosts the early phase of massive star formation, where the presence of an evolved HII region is unlikely. Hence, our selected target site appears to be a perfect HFS candidate, which is not yet affected by UV photons from the HII region.

Acknowledgements

We are thankful to the anonymous reviewer for the useful comments and suggestions. The research work at Physical Research Laboratory, Ahmedabad, is funded by the Department of Space, Government of India. This research made use of the data from the Milky Way Imaging Scroll Painting (MWISP) project, which is a multi-line survey in 12CO/13CO/C18O along the northern galactic plane with PMO-13.7m telescope. We are grateful to all the members of the MWISP working group, particularly the staff members at PMO-13.7m telescope, for their long-term support. MWISP was sponsored by National Key R&D Program of China with grant 2017YFA0402701 and by CAS Key Research Program of Frontier Sciences with grant QYZDJ-SSW-SLH047. This research used the facilities of the Canadian Astronomy Data Centre operated by the National Research Council of Canada with the support of the Canadian Space Agency. CE acknowledges the financial support from grant RJF/2020/000071 as a part of the Ramanujan Fellowship awarded by the Science and Engineering Research Board (SERB), Department of Science and Technology (DST), Government of India.

References

Aguirre J. E., Ginsburg A. G., Dunham M. K., *et al.* 2011, ApJS, 192, 4
André P., Men'shchikov A., Bontemps S., *et al.* 2010, A&A, 518, L102
Bailer-Jones C. A. L., Rybizki J., Fouesneau M., Demleitner M., Andrae R. 2021, AJ, 161, 147
Bally J., Aguirre J., Battersby C., *et al.* 2010, ApJ, 721, 137
Baug T., Ojha D. K., Dewangan L. K., *et al.* 2015, MNRAS, 454, 4335
Baug T., Dewangan L. K., Ojha D. K., *et al.* 2018, ApJ, 852, 119
Bhadari N. K., Dewangan L. K., Ojha D. K., Pirogov L. E., Maity A. K. 2022, ApJ, 930, 169
Bica E., Dutra C. M., Barbuy B. 2003, A&A, 397, 177
Bonnell I. A., Bate M. R. 2006, MNRAS, 370, 488

Bonnell I. A., Bate M. R., Clarke C. J., Pringle J. E. 2001, MNRAS, 323, 785
Bonnell I. A., Vine S. G., Bate M. R. 2004, MNRAS, 349, 735
Buckle J. V., Hills R. E., Smith H., *et al.* 2009, MNRAS, 399, 1026
Carpenter J. M., Heyer M. H., Snell R. L. 2000, ApJS, 130, 381
Chen M. C.-Y., Di Francesco J., Rosolowsky E., *et al.* 2020, ApJ, 891, 84
Condon J. J., Cotton W. D., Greisen E. W., *et al.* 1998, AJ, 115, 1693
Dewangan L. K. 2021, MNRAS, 504, 1152
Dewangan L. K. 2022, MNRAS, 2204.02127
Dewangan L. K., Ojha D. K., Baug T. 2017, ApJ, 844, 15
Dewangan L. K., Ojha D. K., Luna A., *et al.* 2016, ApJ, 819, 66
Dewangan L. K., Ojha D. K., Sharma S., *et al.* 2020, ApJ, 903, 13
Dewangan L. K., Zinchenko I. I., Zemlyanukha P. M., *et al.* 2022, ApJ, 925, 41
Elia D., Schisano E., Molinari S., *et al.* 2010, A&A, 518, L97
Enoch M. L., Evans Neal J., I., Sargent A. I., *et al.* 2008, ApJ, 684, 1240
Fabricius C., Luri X., Arenou F., *et al.* 2021, A&A, 649, A5
Gaia Collaboration Brown A. G. A., Vallenari A., *et al.* 2021, A&A, 649, A1
Ginsburg A., Glenn J., Rosolowsky E., *et al.* 2013, ApJS, 208, 14
Griffin M. J., Abergel A., Abreu A., *et al.* 2010, A&A, 518, L3
Gutermuth R. A., Megeath S. T., Myers P. C., *et al.* 2009, ApJS, 184, 18
Hacar A., Tafalla M. 2011, A&A, 533, A34
Hacar A., Tafalla M., Alves J. 2017, A&A, 606, A123
Hacar A., Tafalla M., Kauffmann J., Kovács A. 2013, A&A, 554, A55
Heyer M. H., Brunt C., Snell R. L., *et al.* 1998, ApJS, 115, 241
Hildebrand R. H. 1983, QJRAS, 24, 267
Kauffmann J., Bertoldi F., Bourke T. L., Evans N. J., I., Lee C. W. 2008, A&A, 487, 993
Kirk H., Myers P. C., Bourke T. L., *et al.* 2013, ApJ, 766, 115
Lada C. J., Bergin E. A., Alves J. F., Huard T. L. 2003, ApJ, 586, 286
Launhardt R., Stutz A. M., Schmiedeke A., *et al.* 2013, A&A, 551, A98
Li Y., Xu Y., Sun Y., *et al.* 2019, ApJS, 242, 19
Liu H.-L., Tej A., Liu T., *et al.* 2022, MNRAS, 511, 4480
Lumsden S. L., Hoare M. G., Urquhart J. S., *et al.* 2013, ApJS, 208, 11
Mallick K. K., Ojha D. K., Tamura M., *et al.* 2015, MNRAS, 447, 2307
McKee C. F., Tan J. C. 2003, ApJ, 585, 850
Men'shchikov A. 2021, A&A, 649, A89
Molinari S., Swinyard B., Bally J., *et al.* 2010, A&A, 518, L100
Motte F., Bontemps S., Louvet F. 2018, ARA&A, 56, 41
Myers P. C. 2009, ApJ, 700, 1609
Nakamura F., Sugitani K., Tanaka T., *et al.* 2014, ApJ, 791, L23
Olmi L., Cunningham M., Elia D., Jones P. 2016, A&A, 594, A58
Ouyang X.-J., Chen X., Shen Z.-Q., *et al.* 2019, ApJS, 245, 12
Padoan P., Pan L., Juvela M., Haugbølle T., Nordlund Å. 2020, ApJ, 900, 82
Rosen A. L., Offner S. S. R., Sadavoy S. I., *et al.* 2020, SSRv, 216, 62
Saito H., Saito M., Moriguchi Y., Fukui Y. 2006, PASJ, 58, 343
Saito H., Saito M., Sunada K., Yonekura Y. 2007, ApJ, 659, 459
Schneider N., Csengeri T., Hennemann M., *et al.* 2012, A&A, 540, L11
Skrutskie M. F., Cutri R. M., Stiening R., *et al.* 2006, AJ, 131, 1163
Su Y., Yang J., Zhang S., *et al.* 2019, ApJS, 240, 9
Tan J. C., Beltrán M. T., Caselli P., *et al.* 2014, in Protostars and Planets VI, eds Beuther H., Klessen R. S., Dullemond C. P., Henning T., 149
Teague R. 2019, Research Notes of the American Astronomical Society, 3, 74
Tigé J., Motte F., Russeil D., *et al.* 2017, A&A, 602, A77
Treviño-Morales S. P., Fuente A., Sánchez-Monge Á., *et al.* 2019, A&A, 629, A81
Vázquez-Semadeni E., Gómez G. C., Jappsen A. K., Ballesteros-Paredes J., Klessen R. S. 2009, ApJ, 707, 1023
Vázquez-Semadeni E., González-Samaniego A., Colín P. 2017, MNRAS, 467, 1313
Vázquez-Semadeni E., Palau A., Ballesteros-Paredes J., Gómez G. C., Zamora-Avilés M. 2019, MNRAS, 490, 3061
Whitney B., Benjamin R., Meade M., *et al.* 2011, in American Astronomical Society Meeting Abstracts, Vol. 217, American Astronomical Society Meeting Abstracts #217, 241.16
Wright E. L., Eisenhardt P. R. M., Mainzer A. K., *et al.* 2010, AJ, 140, 1868
Wu Y., Wei Y., Zhao M., *et al.* 2004, A&A, 426, 503
Zinnecker H., Yorke H. W. 2007, ARA&A, 45, 481